

Photoevaporation from Inner Protoplanetary Disks Confronted with Observations

YIREN LIN,^{1,2} LILE WANG,^{1,2} MIN FANG,^{3,4} AHMAD NEMER,⁵ AND JEREMY GOODMAN⁶

¹*The Kavli Institute for Astronomy and Astrophysics, Peking University, Beijing 100871, China*

²*Department of Astronomy, School of Physics, Peking University, Beijing 100871, China*

³*Purple Mountain Observatory, Chinese Academy of Sciences, 10 Yuanhua Road, Nanjing 210023, China*

⁴*University of Science and Technology of China, Hefei 230026, China*

⁵*Center for Astrophysics and Space Science, New York University Abu Dhabi*

⁶*Department of Astrophysical Sciences, Princeton University, Princeton NJ 08540, USA*

ABSTRACT

The decades-long explorations on the dispersal of protoplanetary disks involve many debates about photoevaporation versus magnetized wind launching mechanisms. This work argues that the observed winds originating from the inner disk ($R \lesssim 0.3$ AU) cannot be explained by the photoevaporative mechanism. Heating the gas to proper temperatures for the observed forbidden lines (especially [O I] 6300 Å) will over-ionize it, suppressing the abundances of species responsible for the emission. Even if adequate emissivity is achieved by fine-tuning the physical parameters, the total cooling power will become unattainable by the radiative heating alone. Energy conservation requires the presumed photoevaporative winds to be heated to $\gtrsim 10^5$ K when launched from inner disks. However, due to efficient thermal accommodation with dust grains and cooling processes at high densities, X-ray irradiation at energies above 1 keV cannot efficiently launch winds in the first place because of its high penetration. Some studies claiming X-ray wind launching have oversimplified the thermochemical couplings. Confirmed by semi-analytic integrations of thermochemical fluid structures, such high ionizations contradict the observed emission of neutral and singly-ionized atoms from the winds originating from the inner disks.

Keywords: Hydrodynamics (1963), Stellar accretion disks (1579), Protoplanetary disks (1300), Exoplanet formation (492)

1. INTRODUCTION

As the birthplaces of planets, protoplanetary disks (PPDs) undergo dispersal through various processes, including planet formation, accretion onto the central protostar, and outflowing in winds. The latter two processes compete with planet formation, limiting the available time and mass for it (Pascucci et al. 2023). Photoevaporation occurs in the absence of magnetic fields, where high-energy photons heat the gas and unbind it from the star (e.g. Alexander et al. 2006a; Gorti & Hollenbach 2009; Owen et al. 2010; Wang & Goodman 2017). These winds only carry off their own share of angular momenta and are not directly related to disk accretion. On the other hand, magnetized winds can

exert torque on the disk and drive accretion. Two types of magnetized winds have been identified: magnetocentrifugal winds and magneto-thermal winds; modeling suggests that the latter type prevails in PPDs (Bai et al. 2016). Numerical studies of magnetized winds and associated accretion demand the consistent inclusion of physical processes related to non-ideal magnetohydrodynamics (MHD) (e.g. Wardle & Königl 1993; Bai & Goodman 2009; Xu & Bai 2016; Bai 2017; Wang et al. 2019). With proper treatments of radiation and subsequent non-equilibrium thermochemistry, “hybrid” winds with photoevaporation based on and spatially located above magnetized outflows were found in Wang et al. (2019), yet the foundations were still the magnetized winds.

Forbidden line emissions from atoms and ions (e.g., [O I] 6300 Å, and [Ne II] 12.8 μ m) have been used as prospective indicators of PPD winds. Researchers have

proposed expected observables and synthetic observations accordingly, based on the photoevaporative wind models (e.g. Alexander et al. 2006b; Alexander 2008; Ercolano & Owen 2016), as well as the magnetized wind models (Nemer et al. 2020). Emerging observations with high spatial and spectral resolution indicate that the broad and generally (and usually slightly) blueshifted low-velocity component (LVC) of [O I] 6300 Å emission come from regions with relatively high densities of neutral materials (Banzatti et al. 2019; Fang et al. 2023a) and fairly close to the central star ($R \lesssim 0.3$ AU for TW Hya, a solar-mass star, Fang et al. 2023b). These results are in favor of the magnetized wind models as they are sufficient to provide adequate physical conditions without being limited by the depths of gravitational potential wells.

Arguments from the photoevaporation side also emerge. Some models, with an emitting and mostly static or circulating corona above the inner disk and photoevaporation winds launched at larger radii, were proposed to claim that photoevaporative winds are also able to explain what has been observed (e.g. Rab et al. 2023, R23 hereafter). However, a circulating corona of gas that does not drive materials to infinity is not an outflow, and should not be defined as a “photoevaporative wind”. Discussions about wind launching mechanisms should not rely on the analyses of inner-disk coronae that are not winds. Meanwhile, the line profiles of the [O I] 6300 emission of various PPDs are generally wide ($\gtrsim 20$ km s⁻¹) and often blueshifted (Fang et al. 2018). Such line profiles are the indications of outflows, rather than the hydrostatic or circulating gas above disk surfaces. This problem is especially unresolvable if the basic assumption about photoevaporation, that the dynamics are driven almost solely by stellar radiation, is made for an inner-disk corona, no matter if it is hydrostatic, in circulation motion, or inside a wind. In what follows, we will use the word “corona” to denote the coronal region above the disk surface in general, no matter it is a photoevaporative wind, hydrostatic gas, or the coronal gas in circulating motion.

This paper focuses on demonstrating the conflicts between the photoevaporative disk wind model and observation results, based on the detailed observations on TW Hya (Fang et al. 2023b) in particular, while also applicable to a broader range of PPDs as well: the inner disk within ~ 1 AU from the host star could not launch photoevaporation with physical consistency, given the observation constraints especially on the luminosity of [O I] 6300 Å emission. Similar concerns have been raised since the discoveries of PPD outflows (e.g. Font et al. 2004), and this work discusses the general conditions

of PPD wind launching from the inner disk using latest observational constrains. The paper is organized as follows. The required thermal conditions concerning neutral oxygen radiation, cooling power, and photoevaporation are described in Section 2, which is one of the core issues conflicting photoevaporation with observation. Section 3 discusses the issue regarding the energetic balance of the inner-disk photoevaporative wind model. Section 4 presents more comprehensive semi-analytic models that exposes those issues quantitatively. The overall conclusions are summarized and discussed in Section 5. Details of several physics issues relevant to the discusses are elaborated in the Appendices.

2. IONIZATION AND EMISSIVITY

The emission of the [O I] 6300 Å line requires neutral oxygen atoms existing at relatively high temperatures ($\gtrsim 5000$ K, but not too hot—otherwise oxygen will be ionized thermally). How much neutral oxygen is needed? For TW Hya, Fang et al. (2023b) reported the luminosity on the emission line $L_{6300} \sim 1.5 \times 10^{-5} L_{\odot} \sim 5.8 \times 10^{28}$ erg s⁻¹. The volume of a sphere with $R = 0.5$ AU is 1.8×10^{39} cm³, which sets the lower limits of the emissivity, $\varepsilon \gtrsim 3 \times 10^{-11}$ erg cm⁻³ s⁻¹. Considering the typical value of elemental abundance of oxygen as $X_{\text{O}} \sim 3 \times 10^{-4}$, such a high emissivity will require oxygen to be predominantly neutral inside the wind if the electrons with density $n_e \gtrsim 10^6$ cm⁻³ all come from the ionization of hydrogen, and $T \gtrsim 10^4$ K.

2.1. Ionization conditions

2.1.1. Lengths and timescales of photoionization

One of the most important destroyers of neutral oxygen is high-energy photons. The “standard” X-ray luminosity used in R23 is $L_X = 2 \times 10^{30}$ erg s⁻¹ $\simeq 5 \times 10^{-4} L_{\odot}$ (also adopted in Wang & Goodman 2017; Wang et al. 2019). The coronal region above the disk surface within $R = 1$ AU standing between the source and wind bases at larger distances, either a hydrodynamic wind or a hydrostatic corona, must be transparent to high-energy photons, otherwise those photons will not reach the disk surface to launch the wind.

The X-ray ionization cross sections of atomic hydrogen and oxygen are, above the inner shell ionization threshold ($h\nu \gtrsim 0.53$ keV; see also the lower panel of Figure 1),

$$\begin{aligned} \sigma_{\text{H},i} &\sim 1.6 \times 10^{-23} \text{ cm}^2 \times \left(\frac{h\nu}{\text{keV}} \right)^{-3}, \\ \sigma_{\text{O},i} &\sim 1.1 \times 10^{-19} \text{ cm}^2 \times \left(\frac{h\nu}{\text{keV}} \right)^{-3}, \end{aligned} \quad (1)$$

which can be applied to estimate the photoionization rate of oxygen and hydrogen, $\zeta_Z \simeq L_X \sigma_{Z,i} / (4\pi R^2 h\nu)$

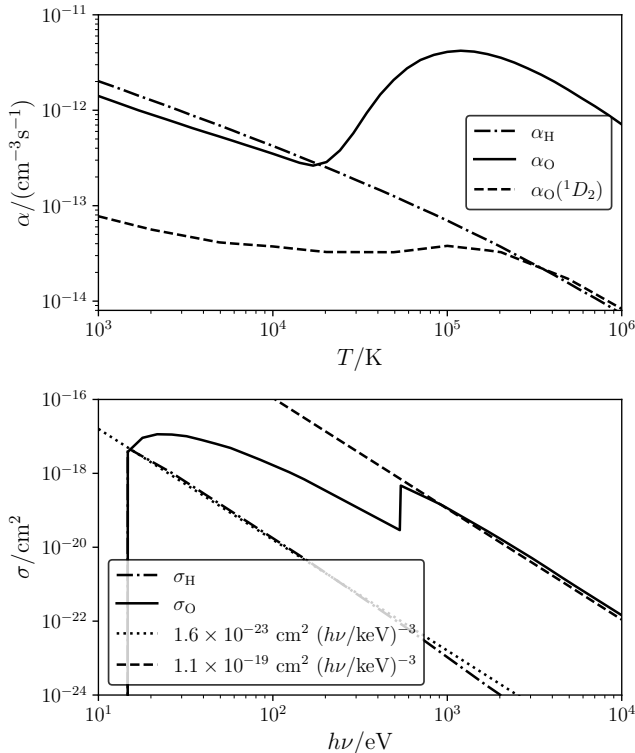


Figure 1. Key atomic data adopted in this work. **Upper panel:** Recombination rates as functions of temperatures (based on Mitnik & Badnell 2004; Summers 2004), presenting the total case B recombination rates α_{H} for H II (dash-dotted curve), α_{O} for O II (solid curve), and $\alpha_{\text{O}}(^1D_2)$ specifically for the recombination to 1D_2 state of O I (dashed curve; populations of O II parent states have been considered). These rates have both radiative and dielectronic recombination components summarized. **Lower panel:** Photoionization cross sections of H I (dashed curve) and O I (solid curve) based on Verner et al. (1996). The power-law approximations are also presented for hydrogen (dotted curve) and oxygen ($h\nu > 530$ eV; dashed curve).

(Z is either O or H). Constrained by the observations, the wind velocity is at the order of $v_w \sim 5$ km s $^{-1}$ (as adopted by R23), leading to the following estimate of the attenuation length of neutral oxygen abundances,

$$\lambda_{\text{O},i} \sim \zeta_{\text{O}}^{-1} v_w \sim 0.062 \text{ AU} \times \left(\frac{L_X}{2 \times 10^{30} \text{ erg s}^{-1}} \right)^{-1} \times \left(\frac{v_w}{5 \text{ km s}^{-1}} \right) \left(\frac{R}{0.3 \text{ AU}} \right)^2 \left(\frac{h\nu}{\text{keV}} \right)^4. \quad (2)$$

In other words, for X-rays with photon energy 1 keV, the abundance of neutral oxygen will decrease by one decade every $(\ln 10) \times \lambda_{\text{O},i} \sim 0.14$ AU as the gas traverses the wind. Only a few times 0.1 AU above the wind base, the neutral fraction of oxygen becomes too

low. Note also that, even if an important fraction of neutral oxygen and hydrogen atoms manage to survive in the inner disk corona, their absorption of ionizing photons will inhibit XUV from irradiating and evaporating the outer disk. This shielding effect undermines the physical picture proposed in R23, which has a static inner corona with a fraction of neutral oxygen and a photoevaporating outer disk.

2.1.2. Ionization and recombination

In view of the short ionizing length for the outflowing gas, ionization equilibrium should establish quickly; hence a lower bound to the ionization fraction can be obtained by balancing *collisional* ionization against recombination. The recombination rate coefficient for the reaction $\text{O II} + e^- \rightarrow \text{O I}$ is described by the total rates in Figure 1. The corresponding collisional ionization rate $\text{O I} + e^- \rightarrow 2e^- + \text{O II}$ (Bell et al. 1983), we have (subscript “ci” for collisional ionization; $T_4 \equiv T/10^4$ K),

$$k_{\text{O,ci}} \simeq 8.7 \times 10^{-9} \text{ cm}^3 \text{ s}^{-1} T_4^{1/2} \exp\left(-\frac{15.81}{T_4}\right). \quad (3)$$

The ionization condition of oxygen is bound by the electron abundance, constrained by the ionization balance of hydrogen, where the recombination rate is also presented in Figure 1, and the collisional ionization rate approximately reads,

$$k_{\text{H,ci}} \simeq 6.4 \times 10^{-9} \text{ cm}^3 \text{ s}^{-1} T_4^{1/2} \exp\left(-\frac{15.78}{T_4}\right). \quad (4)$$

Although charge exchange processes, $\text{O}^+ + \text{H} \leftrightarrow \text{O} + \text{H}^+$, may be important in non-equilibrium calculations, their effects are readily covered by detail balances in equilibrium states. Even in non-equilibrium calculations, at sufficiently high temperatures ($T \gg 228$ K, which corresponds to the difference in ionization energy between H and O), the charge exchange has negligible impacts on the ionization conditions.

Let n_{H} be the total number density of hydrogen $n_{\text{H}} = n(\text{H}) + n(\text{H}^+)$, x_e be the ionized fraction of hydrogen $x_e \equiv n_e/n_{\text{H}}$, and $n(\text{H}) = (1 - x_e)n_{\text{H}}$. We first solve the ionization balance of hydrogen (the negative branch of solution is ignored):

$$\alpha_{\text{H}} n_{\text{H}}^2 x_e^2 - \zeta_{\text{H}} n_{\text{H}} (1 - x_e) - k_{\text{H,ci}} n_{\text{H}}^2 x_e (1 - x_e) = 0. \quad (5)$$

Given the electron number density n_e , the ionization balance of oxygen reads (where x_{O} is the fraction of neutral oxygen compared to total oxygen, $x_{\text{O}} \equiv n(\text{O})/n_{\text{O}}$),

$$\alpha_{\text{O}} n_e n_{\text{O}} (1 - x_{\text{O}}) - \zeta_{\text{O}} n_{\text{O}} x_{\text{O}} - k_{\text{O,ci}} n_e n_{\text{O}} x_{\text{O}} = 0. \quad (6)$$

Solutions to eqs. (5), (6) under different conditions are presented in Figure 2. When $T \gtrsim 3 \times 10^4$ K, the neutral

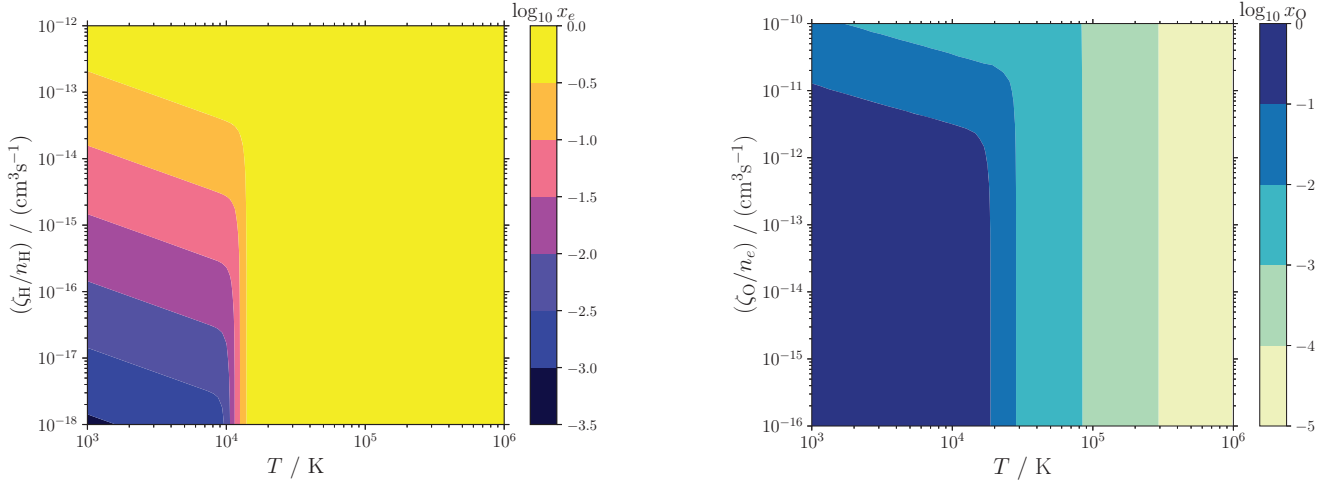


Figure 2. Contour plots for the ionized fraction of hydrogen (left) and neutral fraction of oxygen (right), as functions of (T/K) and $(\zeta_{\text{H}}/n_{\text{H}})/(\text{cm}^3 \text{s}^{-1})$ (left panel) or $(\zeta_{\text{O}}/n_e)/(\text{cm}^3 \text{s}^{-1})$ (right panel). For $T \gtrsim 3 \times 10^4$ K, the ionized fraction is close to 1 and the neutral fraction of oxygen drops to $x_{\text{O}} < 10^{-2}$.

fraction of oxygen drops to $x_{\text{O}} < 10^{-2}$. The neutral fraction will drop even further down to $x_{\text{O}} < 10^{-4}$ at $T \sim 10^5$ K. Such low abundances of neutral oxygen is generally inadequate to yield the observed [O I] 6300 Å emission luminosity. As we will also discuss later in §3.1, the specific thermal energy corresponding to this temperature is also insufficient to drive outflows even from $R = 1$ AU, let alone $R = 0.3$ AU or 0.1 AU.

From Figure 2, one can infer that the biggest hope of obtaining significant fractions of neutral oxygen is to stand close to the lower-left corner, i.e. with low temperatures (T) and weak ionization-electron ratio (ζ_{O}/n_e). However, attempts in this domain will inevitably bog down to the following multilemma. One way to lower ζ_{O}/n_e is to have small ζ_{O} , which means either small L_{X} or strong attenuation of X-ray. Both possibilities will inhibit photoevaporative winds, as this wind launching mechanism requires intensive radiative heating. Another way to lower ζ_{O}/n_e is to have greater n_e . Then here comes another problem: where do the electrons come from?

- If they come mainly from the photoionization of hydrogen (including secondary ionization by electrons or recombination photons in the X-ray ionization cascades), then the photon flux should be large enough to ionize oxygen to a greater extent—remember $\sigma_{\text{O},i}$ is significantly greater than $\sigma_{\text{H},i}$ for X-ray photons ($\sim 10^4$ times at $h\nu = 1$ keV), due to the interactions with inner shell electrons.
- If they are produced via collisional ionization, then the temperature should be high enough to significantly ionize hydrogen—this will also lead to sig-

nificant ionization of oxygen, as their ionization energy values are almost the same.

These issues narrow the possible parameter space for the co-existence of O I, sufficient free electrons, and relatively high temperatures; all of which are necessary for sufficiently luminous [O I] 6300 Å radiation.

2.2. Are sufficient emissivities possible?

Given the Einstein A coefficient $A \simeq 5.63 \times 10^{-3} \text{ s}^{-1}$ (Kramida et al. 2022) of this transition from 1D_2 to 3P_2 , the collisional excitation (subscript “ex”) and de-excitation (“de”) rates are approximately (see also Tielens & Hollenbach 1985; Pequignot 1990; subscripts “H” and “e” indicate the collision partner, neutral hydrogen or free electron),

$$\begin{aligned}
 k_{\text{de},e} &\simeq 4.1 \times 10^{-9} \text{ cm}^3 \text{ s}^{-1} \times \left(\frac{T_4^{0.93}}{1 + 0.605T_4^{1.105}} \right), \\
 k_{\text{de},\text{H}} &\simeq 5.7 \times 10^{-13} \text{ cm}^3 \text{ s}^{-1}, \\
 k_{\text{ex},\text{H},e} &\simeq k_{\text{de},\text{H},e} \frac{g_u}{g_l} \exp\left(-\frac{hc/\lambda}{k_{\text{B}}T}\right).
 \end{aligned} \tag{7}$$

The population fraction of the upper 1D_2 state x_u and the lower 3P_2 state x_l can be estimated by, assuming $x_u + x_l \simeq 1$ and $n(\text{H}) = n_{\text{H}}(1 - x_e)$,

$$\begin{aligned}
 &n(\text{O})x_u[k_{\text{de},e}n_e + k_{\text{de},\text{H}}n(\text{H}) + A] \\
 &\simeq n(\text{O})x_l[k_{\text{ex},e}n_e + k_{\text{ex},\text{H}}n(\text{H})] + \alpha_{\text{O}}(^1D_2)n(\text{O}^+)n_e; \\
 x_u &\simeq \frac{k_{\text{ex},e} + k_{\text{ex},\text{H}}(x_e^{-1} - 1) + \alpha_{\text{O}}(^1D_2)(x_{\text{O}}^{-1} - 1)}{(k_{\text{ex},e} + k_{\text{de},e}) + (x_e^{-1} - 1)(k_{\text{ex},\text{H}} + k_{\text{de},\text{H}}) + An_e^{-1}},
 \end{aligned} \tag{8}$$

where the $\alpha_{\text{O}}(^1D_2)$ values adopted are presented in the upper panel of Figure 1, based on the atomic

physics data in Mitnik & Badnell (2004); Summers (2004). Throughout the temperatures range concerned, one can observe that $\alpha_{\text{O}}(^1D_2) < 10^{-13} \text{ cm}^3 \text{ s}^{-1}$ even with the dielectronic recombination and the cascade from higher recombination products taken into account. The collisional excitation by neutral hydrogen $k_{\text{ex,H}}$ has considerable contribution to the emissivity only when $T < 10^4 \text{ K}$. The solution ignoring these two terms, $x_u \simeq k_{\text{ex,e}}/(k_{\text{ex,e}} + k_{\text{de,e}} + An_e^{-1})$, is a reasonable approximation throughout most of the parameter space concerned.

Using the population number given by eqs. (8), the emissivity through the [O I] line can be estimated by $\epsilon_{6300} = n_{\text{H}}X_{\text{O}}x_{\text{O}}x_uAh\nu_{6300}$ ($h\nu_{6300} = 1.97 \text{ eV}$ is the photon energy of the [O I] 6300 Å emission; not to be confused with the ionizing photon energy $h\nu$). The results are presented in Figure 3, showing highly insufficient emissivity for the $n_{\text{H}} \leq 10^6 \text{ cm}^{-3}$ cases. The $n_{\text{H}} \gtrsim 10^8 \text{ cm}^{-3}$ cases obtain regions in the parameter spaces that yield sufficient ϵ_{6300} , at temperatures $1 \lesssim T_4 \lesssim 2$. These parameters are quite common in magnetized disk wind models with reasonable selection of physical parameters (e.g. Gressel et al. 2015; Bai 2017; Wang et al. 2019; Riols et al. 2020). In contrast, gas heated solely by radiation, either in photoevaporative winds or hydrostatic coronae, will have difficulties to maintain these physical conditions.

Gas at high temperatures ($T_4 > 1$) and high densities ($n_{\text{H}} > 10^8 \text{ cm}^{-3}$) simultaneously are susceptible to significant cooling. The total cooling power in the emitting region reads approximately,

$$L_{\text{cool}} \simeq V_{6300}\Lambda n_e n_{\text{H}} \simeq 5 \times 10^{-3} L_{\odot} \times x_e \left(\frac{V_{6300}}{0.5 \text{ AU}^3} \right) \times \left(\frac{\Lambda}{10^{-24} \text{ erg cm}^3 \text{ s}^{-1}} \right) \left(\frac{n_{\text{H}}}{10^8 \text{ cm}^{-3}} \right)^2. \quad (9)$$

Here V_{6300} is the volume of the emitting region (the volume of an $r = 0.5 \text{ AU}$ sphere is $\sim 0.5 \text{ AU}^3$), and Λ is the cooling rate coefficient. When the gas has relatively high ionization fraction ($x_e \gtrsim 10^{-1}$), the cooling via case B recombination of hydrogen alone yields $\Lambda > 3 \times 10^{-25} \text{ erg cm}^3 \text{ s}^{-1}$. When photoionization is not overwhelming, Lyman- α cooling gives $\Lambda > 10^{-23} \text{ erg cm}^3 \text{ s}^{-1}$ if optically thin (e.g. Gnedin & Holton 2012), or effectively $\Lambda \gtrsim 10^{-25} \text{ erg cm}^3 \text{ s}^{-1}$ if optically thick (see also the Monte Carlo simulations for optically thick Lyman- α radiative transfer with similar gas densities, e.g. Ge & Wise 2017). Inclusion of other cooling mechanisms will only make L_{cool} greater. Such a dense and hot corona will radiate at power $L_{\text{cool}} \gtrsim 10^{-3} L_{\odot}$, which requires fairly powerful heat-

ing comparable to the total X-ray power of typical T Tauri stars. For magnetized disk winds that can power the wind gas the extraction of disk gravitational energy via accretion, the upper limit of power injected into the winds, P_{max} , approximately reads,

$$P_{\text{max}} \sim \frac{GM_*\dot{M}_{\text{acc}}}{R} \sim 3 \times 10^{-3} L_{\odot} \left(\frac{\dot{M}_{\text{acc}}}{10^{-8} M_{\odot} \text{ yr}^{-1}} \right) \left(\frac{R}{0.5 \text{ AU}} \right)^{-1}, \quad (10)$$

where M_* is the mass of the protostar, \dot{M}_{acc} is the accretion rate, and the R here describes the typical radial location of wind gas heating. While the magnetized wind is sufficient to power a hot and dense corona, radiation alone seems questionable.

Is it possible to maintain the temperature of such a dense corona by stellar radiation alone? Optical and infrared radiation, carrying most energy from the central protostar, cannot heat the gas beyond the blackbody temperature of the stellar photosphere due to the second law of thermodynamics. What is more, if an $r \sim 0.5 \text{ AU}$, $T \sim 10^4 \text{ K}$ gas sphere is optically thick in optical and infrared bands, one can get, by the Stefan-Boltzmann law, a ridiculous $L_{\text{cool}} \sim 10^5 L_{\odot}$ cooling luminosity. High-energy photons face a different dilemma. If the radial optical depth is low for a band of radiation, energy deposition for photons in this band will be very inefficient. On the other end, high optical depths prevent photons from reaching anywhere beyond the innermost part of the corona. This will stop the radiative heating for most of the coronal gas, and removes the energy source for photoevaporative winds at larger disk radii described in R23. The radial column density of an $n_{\text{H}} = 10^8 \text{ cm}^{-3}$ coronal gas over an 0.5 AU radial line is $N_{\text{H}} \sim 10^{21} \text{ cm}^{-2}$, which is too high for EUV if the neutral fraction is $(1 - x_e) \gtrsim 10^{-3}$, and too low otherwise (for EUV with very low neutral fraction, and for X-ray and FUV). The only possibility is to restrict the physical parameters so that the radial optical depth of the corona is at the order of unity for X-ray, yet this will raise the cooling power to $L_{\text{cool}} \gtrsim L_{\odot}$ due to the increase of n_{H} . More generally speaking, such fine-tuning significantly undermines the capability and robustness of any theoretical models.

3. ENERGETICS OF THE OUTFLOWS

In addition to the thermochemical issues, the energy balance also challenges the mechanisms of wind launching from the inner disk. As multiple observations have figured out, the low-velocity components (LVC) of

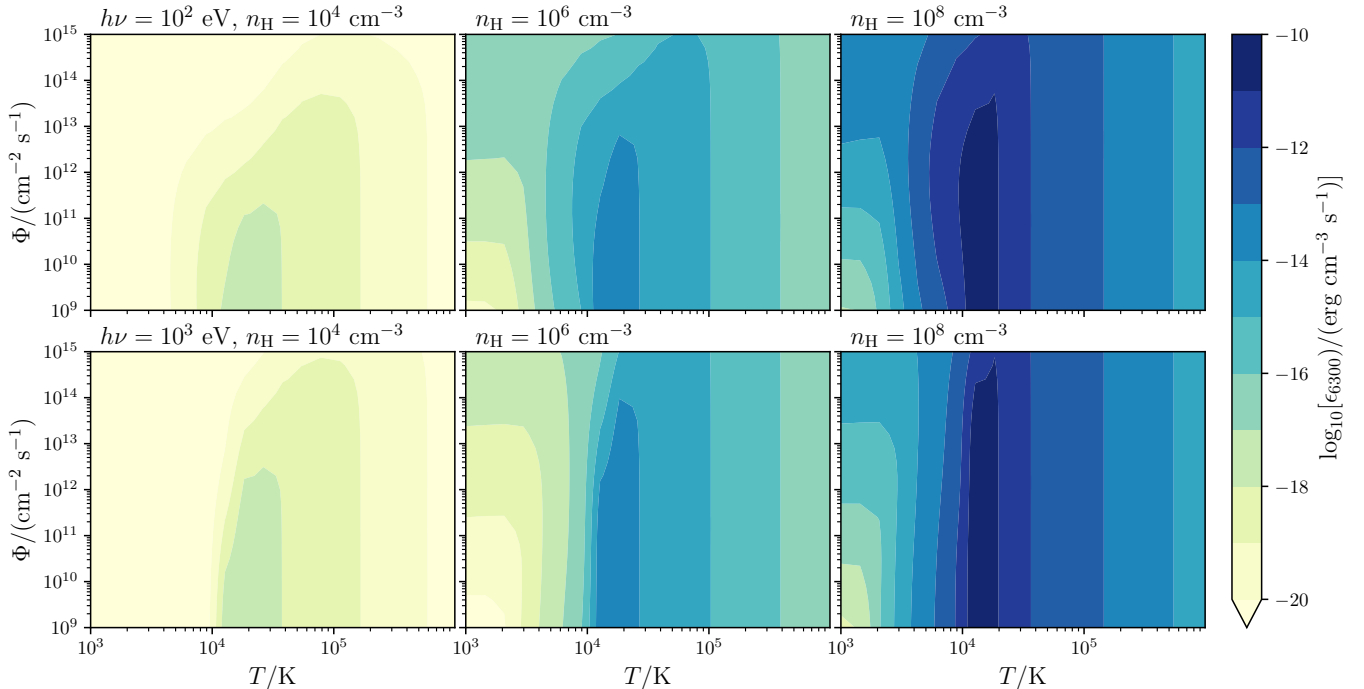


Figure 3. Emissivity of the [O I] 6300 Å line under different radiation fluxes (Φ for the fluxes of ionizing photons) and temperatures, calculated by solving eqs. (8) (§2.2). The upper row presents the results for ionizing photon energy $h\nu = 10^2$ eV, and the lower row for $h\nu = 10^3$ eV. Different gas density values, quantified by the total hydrogen nuclei number density n_{H} , are used in different columns as denoted.

[O I] 6300 Å emission from PPDs are often blueshifted (e.g. Fang et al. 2018; Banzatti et al. 2019; Fang et al. 2023a,b). This is a strong indication that the emission regions are located inside outflows rather than a hydrostatic corona.

In general, gas has to be heated sufficiently to escape from the stellar potential well. As a reference, the wind mass-loss rate \dot{M} is approximately related to the wind parameters (here μ is the mean molecular mass, v_{w} is the wind speed, and n_{H} is the total number density of hydrogen nuclei),

$$\dot{M} \sim 0.4 \times 10^{-9} M_{\odot} \text{ yr}^{-1} \times \left(\frac{n_{\text{H}}}{10^7 \text{ cm}^{-3}} \right) \left(\frac{\mu}{m_{\text{p}}} \right) \left(\frac{R}{\text{AU}} \right)^2 \left(\frac{v_{\text{w}}}{5 \text{ km s}^{-1}} \right). \quad (11)$$

3.1. Gravitational potential and the escape

Is the heating enough for gas to escape the stellar potential well? We begin with the assumption of instantaneous injection of radiation energy for simplicity and a more realistic scenario will be elaborated in §4.

Under the hydrodynamic conditions (Appendix A), the velocity of fluid particles is thermalized, and the thermal energy has to be greater than the potential well depth to escape. Considering the fact that the gas in an protoplanetary disk orbits the central star at a velocity very close to the local Keplerian speed

$v_{\text{K}} \equiv (GM_{*}/R)^{1/2}$, the effective depth of the potential well satisfies (ε_k is the specific kinetic energy),

$$|\phi| \simeq |\Phi + \varepsilon_k| \simeq \left| -\frac{GM_{*}}{R} + \frac{v_{\text{K}}^2}{2} \right| = \frac{GM_{*}}{2R} \simeq 4.6 \text{ eV } m_{\text{p}}^{-1} \times \left(\frac{R}{\text{AU}} \right)^{-1} \left(\frac{M_{*}}{M_{\odot}} \right). \quad (12)$$

Even if significant flaring raises the altitude of the wind base, one can easily prove that,

$$|\phi|_{\theta} = \left| -\frac{GM_{*}}{R/\cos\theta} + \frac{v_{\text{K}}^2}{2} \cos^3\theta \right| = |\phi| \cos\theta (1 + \sin^2\theta), \quad (13)$$

where θ is the flaring angle (the angle between the vector from the star to the wind base and the equatorial plane). Compared to more complete calculations that involve consistent azimuthal velocity v_{ϕ} , this estimation is still approximately valid. The relative deviation from the mid-plane Keplerian speed is roughly $\Delta v_{\phi}/v_{\text{K}} \simeq -(h/R)^2(z/h)^2/2$ (e.g. Takeuchi & Lin 2002), whose absolute value is less than 10 % near the flared disk surface where $z/r \sim 4$. In addition, the consistent v_{ϕ} is slower than v_{K} , and the estimation in eq. (13) stands on the safe side by underestimating $|\phi|_{\theta}$. The factor $f_{\theta} \equiv \cos\theta(1 + \sin^2\theta)$ satisfies $f_{\theta} \in (7/8, 4\sqrt{6}/9)$ when $\theta \in [0, \pi/3]$, and decreases to $f_{\theta} < 0.5$ only when

$\theta > 1.3$. Disk flaring does *not* make the potential well appreciably shallower, because the steady-state specific kinetic energy also decreases at higher altitudes. Given the depth of the potential well, the analysis of energy constraints on the heated outflows can be qualitatively divided into two limiting cases: ballistic motion (or most equivalently, adiabatic), and isothermal.

On the ballistic motion limit, an adiabatic parcel of heated gas receives no more energy injection after heating processes near the wind bases. When it tries to escape from the surface of a protoplanetary disk at $R = 1$ AU, the specific thermal energy of the gas must be at least $\varepsilon_g > |\phi| = 4.6$ eV/ m_p . Considering fully ionized hydrogen plasma, this is equivalent to $\gtrsim 2.3$ eV energy per particle due to equipartition of energy, which is equivalent to $3k_B T/2 \gtrsim 2.3$ eV, or $T \gtrsim 1.8 \times 10^4$ K. This temperature significantly suppresses the neutral fraction of oxygen down to $\sim 10^{-2}$ even in absence of photoionization (see discussions in §2), leading to the insufficiency of neutral oxygen atoms. When coming to the inner sub-AU region as indicated by Fang et al. (2023b), high temperatures at least $T \gtrsim 1.8 \times 10^5$ K are required. At such temperatures, x_O will be suppressed down to $x_O \lesssim 3 \times 10^{-4}$ (see also Figure 2). Note also that the discussions are about fully ionized plasma with small μ . In case of neutral or even molecular gas discussed in R23, the situation will become even worse.

One may be concerned by the photons in the X-ray band, which seem to have greater photon energies than the potential well depths. As we elaborate in Appendix B, photons are even more incapable of heating the gas to the temperature required by the photoevaporative outflows due to their high penetration. One might also be curious about why the photoevaporative winds still seem to be launched from the inner disk in some previous works given the potential well depths (e.g., Ercolano & Owen 2016, R23). We discuss this issue in Appendix C, emphasizing that the oversimplified treatments of gas thermodynamics (by mapping the temperature to the ionization parameter) could always lead to wind launching even when the heated gas is not sufficiently energetic to escape.

3.2. Isotropic isothermal outflows

The other limit is an isothermal outflow, which often results from efficient heating and thermal transfer. While the escape of adiabatic gas requires $|\phi| \lesssim k_B T/\mu$, isothermal coronae always launch outflows (e.g. Parker 1958). The key to estimate the isothermal wind mass-loss rate is the mass density at the sonic critical point ρ_s using the isothermal sound speed c_s and the mass

density at the wind base ρ_b ,

$$\frac{\rho_s}{\rho_b} \sim \exp\left(-\frac{|\phi_b|}{c_s^2}\right) \simeq \exp\left(-\frac{GM_*}{r_b c_s^2}\right), \quad (14)$$

which can be derived from the hydrostatics of gravitated isothermal spheres. This is a reasonable approximation in the subsonic regions, and the error of estimated mass-loss rates is no more than ~ 50 % as one can verify with the standard Parker wind mode. The sonic critical radius roughly reads $r_s \sim GM_*/(2c_s^2) \simeq 5$ AU for gas at 10^4 K escaping from a solar-mass star. The mass-loss rate is related to ρ_s by,

$$\rho_s \simeq \frac{\dot{M}}{4\pi r_s^2 c_s} \simeq 10^{-18} \text{ g cm}^{-3} \times \left(\frac{\dot{M}}{10^{-9} M_\odot \text{ yr}^{-1}}\right). \quad (15)$$

Using eq. (14), one gets $n_{H,b} = 10^{10\sim 11} \text{ cm}^{-3}$ for $r_b \sim 1$ AU, or $n_{H,b} \sim 10^{21} \text{ cm}^{-3}$ for $r_b \sim 0.3$ AU. While the former is on the high end of the possible range, the latter is far beyond any realistic PPD gas.

4. COMPREHENSIVE SEMI-ANALYTIC MODELS

The analyses in §2 and §3 have discussed the energy issues from both aspects of thermochemistry and hydrodynamics, respectively. These approaches may have a limitation: the localized energy injection and subsequent ballistic motion of gas may not fully account for the changes in circumstances that occur when gas moves outwards. This section integrates the physics of both thermochemistry and hydrodynamics for more comprehensive discussions, guided by the typical geometry of disk photoevaporation depicted in Figure 4.

For simplicity, we adopt the estimation method for hydrodynamic outflow profiles based on the hydrostatic equations. This approach has been adopted by various early works on stellar outflows, and here we show that such estimations err on the safe side. Consider the radial momentum equation along a “flux tube” spanned by a streamline and its neighbors (see Figure 4), under the steady state [$\partial(\rho v)/\partial t \equiv 0$],

$$\partial_R p = -\rho v_R \partial_R v_R - \frac{GM_* \rho}{R^2}. \quad (16)$$

With $v_R > 0$ and $\partial_R v_R > 0$ as the gas accelerates before reaching the sonic point, the hydrodynamic solutions always have more negative $\partial_R p$ than the hydrostatic solutions with $v_R = 0$. By integrating from the same wind launching point to the same radius R for p , the pressure profile estimated by hydrostatics is always higher than the actual hydrodynamic values. If one assumes that the outflows are isothermal, the hydrostatic approximation (through multiplying the density at sonic point by

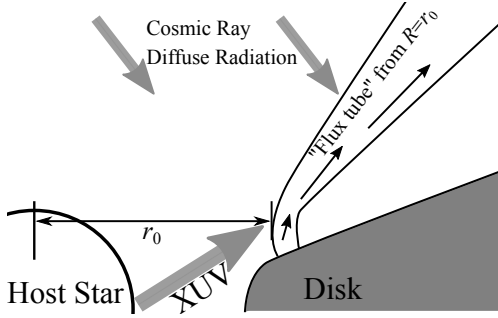


Figure 4. Schematic setups for the semi-analytic models (§4), showing an XUV irradiated “flux tube” originating from $R = r_0$.

the sound speed) will overestimate the mass-loss rate ($\dot{M}_{\text{stat}} > \dot{M}_{\text{dyn,iso}}$). Once the thermodynamics inside outflows are closer to adiabatic rather than isothermal, the actual mass-loss rate will be even lower than the isothermal case ($\dot{M}_{\text{dyn,iso}} > \dot{M}_{\text{dyn}}$). In other words, if the hydrostatic estimations yield a small mass-loss rate, one should expect that the actual wind mass-loss rate is even lower.

4.1. Formulations of the Coronal hydrostatics

Figure 4 illustrates that the fluid geometry can be described by fluid “flux tubes”, which have approximately the same solid angle at different radii, for both the static fluids stalled above a point of the disk surface, and the wind launched from a point on the disk. The guiding equations can be written for the hydrostatic with thermochemistry and radiation in one dimension in spherical geometry,

$$\begin{aligned}
 0 &= \partial_R p + \frac{GM_* m_{\text{H}} n}{R^2}, \\
 p &= n(1 + x_e) k_{\text{B}} T, \\
 0 &= \alpha_{\text{H}} x_e^2 - \frac{F \sigma_{\text{H},i}}{n} (1 - x_e) - k_{\text{H,ci}} x_e (1 - x_e), \quad (17) \\
 0 &= \frac{F \sigma_{\text{H},i}}{n} (1 - x_e) (h\nu - I_{\text{H}}) - \Lambda, \\
 0 &= \partial_R \ln F + \left[\frac{2}{R} + n \sigma_{\text{H},i} (1 - x_e) \right].
 \end{aligned}$$

Here, F is the photon number flux of the XUV photons. Eqs. (17) are solved in their dimensionless forms with the following dimensionless transforms (where we use $n_0 \equiv 1/(\sigma_{\text{H},i} r_0)$ for the reference number density, and $k_0 \equiv 10^{-8} \text{ cm}^3 \text{ s}^{-1}$ for the fiducial rate coefficient),

$$\begin{aligned}
 \zeta &\equiv \frac{R}{r_0}, \quad \varrho \equiv \frac{n}{n_0}, \quad \varpi \equiv \frac{pr_0}{GM_* m_{\text{H}} n_0}, \quad \Theta \equiv \frac{k_{\text{B}} T}{I_{\text{H}}}, \\
 \varphi &\equiv \frac{F \sigma_{\text{H},i}}{n_0 k_0}, \quad \epsilon \equiv \frac{h\nu}{I_{\text{H}}}, \quad \Gamma \equiv \frac{I_{\text{H}} r_0}{GM_* m_{\text{H}}}. \quad (18)
 \end{aligned}$$

The collisional ionization and recombination rates are reduced to dimensionless functions (see also eqs. 4),

$$\begin{aligned}
 k_{\text{H,ci}} &\equiv k_0 \kappa(\Theta), \quad \kappa(\Theta) \simeq 2.3 \Theta^{1/2} e^{-1/\Theta}; \\
 \alpha_{\text{H}} &\equiv k_0 A(\Theta), \quad A(\Theta) \simeq 3.2 \times 10^{-6} \Theta^{-0.75}. \quad (19)
 \end{aligned}$$

The cooling term is decomposed into three components: collisional ionization cooling (Λ_{ci}), recombination cooling (Λ_{rec}), and Lyman α cooling ($\Lambda_{\text{Ly}\alpha}$). These terms are also reduced into their dimensionless forms (see also Murray-Clay et al. 2009, Black 1981),

$$\begin{aligned}
 \Lambda_{\text{rec}} &\equiv \lambda_{\text{rec}}(\Theta) x_e^2 \times I_{\text{H}} k_0, \\
 \Lambda_{\text{Ly}\alpha} &= \lambda_{\text{Ly}\alpha}(\Theta) x_e (1 - x_e) \times I_{\text{H}} k_0, \\
 \Lambda_{\text{ci}} &= \kappa(\Theta) x_e (1 - x_e) \times I_{\text{H}} k_0; \quad (20) \\
 \lambda_{\text{Ly}\alpha}(\Theta) &\simeq \frac{3.44}{1 + 1.26 \Theta^{1/2}} \exp\left(-\frac{3}{4\Theta}\right), \\
 \lambda_{\text{rec}}(\Theta) &\simeq (0.569 - 0.0416 \ln \Theta) \Theta A(\Theta).
 \end{aligned}$$

The total cooling is decomposed into $\Lambda = \Lambda_{\text{ci}} + \Lambda_{\text{rec}} + \beta \Lambda_{\text{Ly}\alpha}$, where the β factor is the escape probability of cooling Ly α photons. It is also noted that the set of cooling processes involved is far from being complete. By setting a default $\beta \rightarrow 0$ and ignoring all other cooling processes, the gas becomes less bound, making them easier to escape and putting us on the safe side by exaggerating the effect opposing to our conclusions.

With such transforms, the dimensional eqs. (17) are recast into the dimensionless form,

$$\begin{aligned}
 \partial_{\zeta} \varphi &= -[2\zeta^{-1} + \varrho(1 - x_e)] \varphi, \\
 \partial_{\zeta} \varpi &= -\zeta^{-2} \varrho, \\
 0 &= \varphi \varrho^{-1} (1 - x_e) + \kappa(\Theta) x_e (1 - x_e) - A(\Theta) x_e^2, \\
 0 &= \varphi \varrho^{-1} (1 - x_e) (\epsilon - 1) - \lambda_{\text{rec}}(\Theta) x_e^2 \\
 &\quad - [\kappa(\Theta) + \beta \lambda_{\text{Ly}\alpha}(\Theta)] x_e (1 - x_e), \\
 \varpi &= \Gamma(1 + x_e) \varrho \Theta. \quad (21)
 \end{aligned}$$

Two extra constraints are required when solving the algebraic part of these equations. First, the carbon element should be predominantly ionized, due to the FUV photons (with $h\nu > 11.2 \text{ eV}$) from the central star and the diffuse interstellar radiation fields. A lower bound $x_{e,\text{min}} = X_{\text{C}}$ should be imposed, and we choose $X_{\text{C}} = 1.4 \times 10^{-4}$. Second, the optical and infrared radiation from the host star also imposes a lower limit on the gas temperature,

$$T_{\text{min}} \simeq T_{\text{eq}} = 886 \text{ K} \times \left(\frac{L_*}{L_{\odot}} \right)^{1/4} \left(\frac{R}{0.1 \text{ AU}} \right)^{-1/2}. \quad (22)$$

Here T_{eq} is the equilibrium temperature of black bodies. We choose the bolometric luminosity $L_* = L_{\odot}$ in this

work, and determine the lower bound for T (and for Θ subsequently) according to the distance to the star. Meanwhile, the ionization by cosmic ray can also be non-negligible when the density is sufficiently low, and we include an extra $\zeta_{\text{CR}} = 10^{-17} \text{ s}^{-1}$ as another ionization source in addition to the central star irradiation.

4.2. Properties of the Solutions

Eqs. (21) can be solved with semi-analytic methods by selecting a set of physical parameters and inner boundary conditions at r_0 . The solutions can be roughly categorized into three types:

- Gravitationally bound. When the injected irradiation has tiny thermochemical impacts, the situation is similar to an externally gravitated polytrope: all gas is gravitationally bound and has no outflows, the system will have a surface (at which the gas density and pressure vanish) at a finite radius.
- Pressure bound. When the gas pressure converges to a constant value (“terminal pressure”) at infinite distances (similar to isothermal atmospheres gravitated by the central star), and such a constant value is lower than the ISM pressure ($\sim 4 \times 10^{-13} \text{ dyn cm}^{-2}$ for both warm and cool neutral media; see [Jenkins & Tripp 2011](#)).
- Unbound. When the terminal pressure is greater than the surroundings.

When the gas is bound, the gas cannot reach infinity and eventually falls back to the disk, which is not a “wind” or “outflow” by definition. In the unbound case, one should in principle connect a steady-state hydrodynamic solution to a hydrostatic solution at a specific point (often called “wind base”). Nevertheless, such problems are always underdefinite when connecting a hydrostatic solution to hydrodynamic solutions analytically (e.g. [Wang & Dai 2018](#)), and the hydrodynamic part is always numerically stiff and less trustworthy. Therefore, we estimate the most important parameter for outflows—the mass-loss rates—by $\dot{M} = 4\pi r_s^2 c_s \rho_s$, in which r_s , c_s , and ρ_s are the radius, sound speed, and mass density at the sonic critical radius where the radial outflow becomes supersonic. Since the actual mass density at the critical radius is certainly less than the hydrostatic estimation because of gas acceleration, this simplification is over-estimating the mass-loss. Such \dot{M} is an extrapolation of a flux tube to the full 4π solid angle, which also lead to an over-estimation due to the geometry (see also Figure 4).

For a perfectly isothermal Parker wind ([Parker 1958](#)), r_s is located at $r_s = GM_*/2c_s^2$. The models described by eqs. (21) have variable temperatures. We thus define a dimensionless Bernoulli parameter,

$$\mathcal{B} \equiv \gamma\varpi/(\gamma - 1) - \varrho/\zeta \quad (23)$$

here γ is the adiabatic index and $\gamma = 5/3$ in all relevant cases in this work. When a solution is gravitationally bound, its \mathcal{B} is always negative. The unbound solutions, in contrast, have transition points from negative \mathcal{B} to positive \mathcal{B} , and we approximate the sonic critical point and associated physical quantities by this transition. Note that there are also cases whose \mathcal{B} becomes positive but pressure converges to very low values at large radii.

4.3. Ionized Corona Solutions

Two solutions with typical selections of physical parameters are presented in Figure 5 showing an unbound solution with XUV (X-ray and extreme ultraviolet) photon energy $h\nu = 300 \text{ eV}$, and a bound solution with $h\nu = 30 \text{ eV}$. The unbound model exhibits a sign transition in the Bernoulli parameter \mathcal{B} at $R \sim 1 \text{ AU}$ (eq. 23), at which the mass density already drops by a factor $\lesssim 10^{-5}$ compared to n_0 . The sound speed at that location, corresponding to the temperature $T \sim 2 \times 10^4 \text{ K}$, is around $\sim 12 \text{ km s}^{-1}$, yet the low mass density leads to a negligible mass-loss rate $\dot{M} \lesssim 10^{-12} M_\odot \text{ yr}^{-1}$. To quantify the significance of wind mass loss, the local wind mass-loss timescale τ_{wind} is defined as,

$$\tau_{\text{wind}} \sim \frac{dM/d \ln R}{d\dot{M}/d \ln R} \simeq \frac{2\pi R^2 \Sigma}{\dot{M}}, \quad (24)$$

where Σ is the disk surface density. Taking $\Sigma \simeq 2 \times 10^3 \text{ g cm}^{-3}$ at $R = 0.3 \text{ AU}$, one gets $\tau_{\text{wind}} \sim 10^8 \text{ yr}$, which is significantly longer than the disk lifetime ($\lesssim 10^7 \text{ yr}$), and dwarfs the importance of photoevaporative wind mass loss. The other model is bound as the energy injection by the $h\nu = 30 \text{ eV}$ photons is insufficient for the gas to escape.

For both models, we calculate the radial distribution of [O I] 6300 Å emissions via calculating the neutral fraction of oxygen (eq. 6). Both models have most of their [O I] emission concentrated near the center ($r \lesssim 0.5 \text{ AU}$), and the unbound model appears to be able to yield sufficient [O I] emission within the $R \lesssim 1 \text{ AU}$ spatial range ($\sim 10^{-5} L_\odot$ for the unbound model, and $\sim 10^{-6} L_\odot$ for the bound model). Nevertheless, the mass-loss rates are tiny or even vanishing, with our simplifications over-estimating the \dot{M} . The velocities of gas with considerable [O I] 6300 emission, which are lower

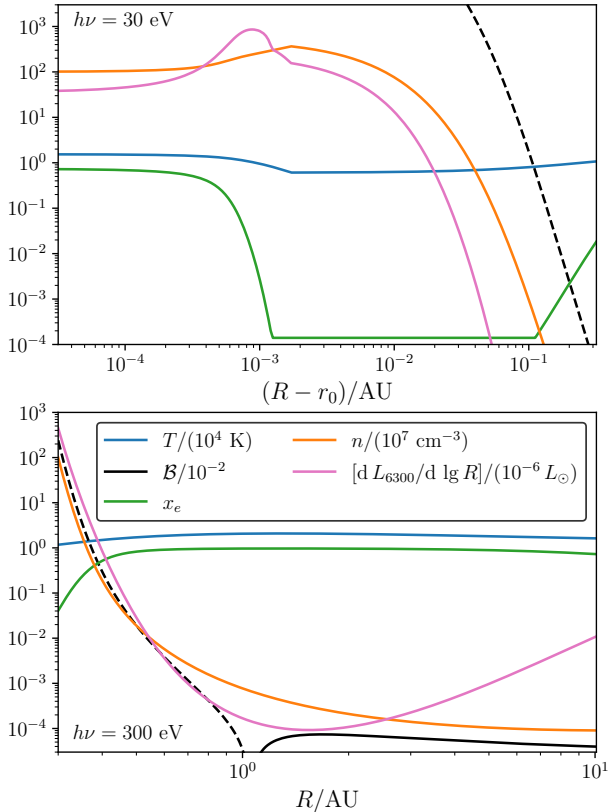


Figure 5. Example solutions for a bound model (upper panel; note that its horizontal axis is $R - r_0$) and an unbound model (lower panel), showing the hydrostatic and thermochemical profiles (distinguished by colors). The [O I] emissions are presented in the luminosity per logarithm radius. Both models have the same key parameters ($M_* = M_\odot$, $r_0 = 0.3$ AU, $n_0 = 10^9$ cm $^{-3}$, $L_{\text{XUV}} = 10^{-3} L_\odot$), with one exception: the bound model has XUV photon energy $h\nu = 30$ eV, while the unbound model has $h\nu = 300$ eV. The Bernoulli parameters (§4.2) are presented in dashed lines when negative and in solid lines when positive.

than the local sound speed, are also slower than adequate to explain the observed blueshifts and line widths of the low velocity components (e.g. Fang et al. 2018, 2023a,b).

One may find some subtle agreements between the above results and Figure 3 in R23. The claimed [O I] emission in R23 comes from a sub-au region with a negligible velocity field, with winds launched just outside and inside this [O I] emitting region. This proposal, nevertheless, resolves neither the dilemma of neutral oxygen versus free electrons nor the problem of excessive cooling. Since the debate mainly focuses on the wind launching, the proposed nearly static region is still inadequate to conclude that the [O I] emission is consistent

with photoevaporative winds if one does not ignore the mass conservation and the sources of streamlines.

Other possible values of physical parameter are explored in Figure 6, showing the mass-loss rates (\dot{M}) and the [O I] luminosities within the innermost 1 AU ($L_{6300,\text{AU}}$) for various XUV luminosities, XUV photon energies, and the radii and the mass densities at the inner radial boundaries. Figure 6 reveals that almost all models with $n_0 < 10^{10}$ cm $^{-3}$ give insufficient mass-loss rates even with excessive, unphysical XUV luminosities (up to $10^{-1} L_\odot$). In fact, such a high density ($n_0 \sim 10^{10}$ cm $^{-3}$) at the wind base is very unlikely. Lifting dense gas to the disk surface requires significant heating below the disk surfaces, which is almost impossible due to the photoevaporative wind geometry and the significant cooling at relatively high densities (see also §2.2, and Appendix C). In addition, for $h\nu \gtrsim 300$ eV photons, the coronal gas near r_0 is predominantly neutral (e.g., Figure 5), and excessively high n_0 will cause considerable absorption at $r \gtrsim 0.3$ AU (see also eq. B2). Numerical simulations have also confirmed that the wind should never be so dense (e.g. Wang & Goodman 2017). Even when the wind is driven by the non-ideal magnetohydrodynamic mechanisms and is relatively slow and dense, the wind-base density is still typically $n_0 \lesssim 10^8$ cm $^{-3}$ (e.g. Bai 2017; Wang et al. 2019). Therefore, the gas should never be as dense as $n_0 \gtrsim 10^{10}$ cm $^{-3}$ at the beginning of the flux tube in the disk corona or even near the disk surface, and the mass-loss rates within 1 AU should be insufficient (i.e., $\ll 10^{-9} M_\odot$ yr $^{-1}$) in the first place. Such results are also consistent with the estimations in §3.1.

One may notice a dilemma emerging from the models presented in Figure 6: a photoevaporative disk cannot produce sufficient [O I] emissions within ~ 1 AU while maintaining adequate mass-loss rates. The models with $r_0 = 1$ AU and $h\nu \gtrsim 300$ eV seem to resolve such a dilemma, yet Fang et al. (2023b) have already indicated that the [O I] emission is concentrated within the innermost sub-au region. Such a dilemma confirms the arguments in §2, §3, and especially §2.2. Photoionization must make its choice between the energy injection and the neutral fraction: an unbound model with adequate mass-loss rates always has high ionized fractions and low emissivities from neutral oxygen, and vice versa. It is worth noting that these models have underestimated the cooling processes. Incorporating these complexities will further bound the gas or reduce the mass-loss rates, confirming the dilemma with higher confidence.

5. SUMMARY

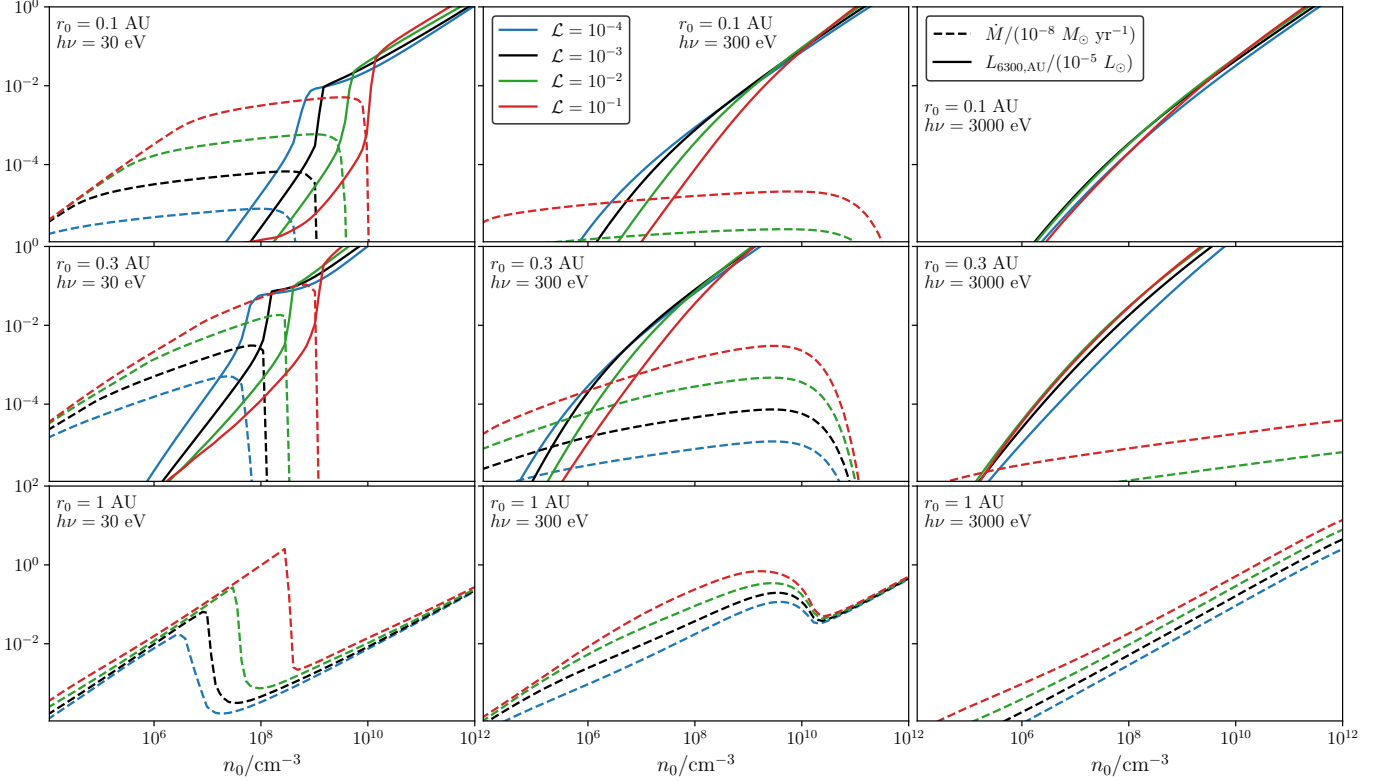


Figure 6. Photoevaporative mass-loss rates (\dot{M} , dashed lines) and [O I] 6300 Å luminosities (solid lines) within $R < 1$ AU ($L_{6300,\text{AU}}$) with different physical parameters: inner boundary radius r_0 , inner boundary hydrogen nuclei number density n_0 , XUV luminosity $\mathcal{L} \equiv L_{\text{XUV}}/L_{\odot}$, and XUV photon energy $h\nu$. Different \mathcal{L} are distinguished by colors in each panel as noted. Various selections of inner radius r_0 and XUV photon energy $h\nu$ are presented in different panels. Note that $L_{6300,\text{AU}}$ vanishes for models with $r_0 = 1$ AU.

In this work, we delve into the inner corona, viz., the gas above the disk surfaces in the inner regions ($R < 1$ AU) of PPDs, explicitly focusing on several major issues that could undermine photoevaporation models when confronted with the observed [O I] 6300 Å emission from the innermost regions of PPDs.

A series of issues emerge from the thermochemistry of inner coronae emitting in [O I] 6300 Å. To yield the $L_{6300} \sim 10^{-5} L_{\odot}$ luminosity observed by e.g. Fang et al. (2023b) within a $r = 0.5$ AU sphere, the coronal gas has to retain sufficient free electrons and neutral oxygen atoms simultaneously at a relatively high ($T \gtrsim 10^4$ K) temperature. The parameter space allowed is pretty narrow, requiring high gas density ($n_{\text{H}} \gtrsim 10^8 \text{ cm}^{-3}$) and proper temperature [$0.5 \lesssim (T/10^4 \text{ K}) \lesssim 2$]. These conditions pose stringent constraints on photoevaporation models, as driving and heating the gas by the high-energy radiation alone are quite impossible due to excessive cooling and thermal exchange (with dust grains). Meanwhile, the cooling power under such conditions is no less than the total X-ray luminosity of a typical protostar, making the issue almost impossible to resolve.

In contrast, the magnetized wind model can stay inside the proper parameter sub-space under a reasonable selection of physical parameters, and the accretion power extracted from the disk accretion is sufficient to maintain the required thermochemical conditions.

The other major issue lies in the energetics of the outflows. We specifically note that the blueshifted [O I] 6300 Å LVC is an indication of non-hydrostatic coronae, and the circulation motion of gas powered by radiative heating inside disk coronae should *not* be described as “photoevaporative winds”. Since the potential well depth at the $R < 0.3$ AU inner disk is deeper than ~ 15 eV, X-ray photons are required to heat the gas to adequately high temperatures to escape. However, because of their excessively high penetration, X-ray photons can only deposit their energy deeply below the disk surfaces; at this point, the thermal coupling between gas and dust grains is tight, and heating to the required temperature is impossible. Insufficient heating makes it impossible for the gas to leave the disk potential well, assuming it will experience ballistic motion after instantaneous energy injection. Even if one assumes that the

heating is continuous along the way out from the potential well, hydrodynamic laws will yield unphysically high density at wind bases.

The analyses from two different aspects tend to exclude photoevaporation models from the explanation the inner-region [O I] 6300 Å profiles. A more complex model, in which a compact [O I] emitting hydrostatic or circulating corona co-exists with photoevaporation winds launched at larger disk radii, cannot bridge the [O I] emission to the photoevaporative winds from the inner disk. To add to the consistency and completeness of the analyses, we construct comprehensive semi-analytic models with the inclusion of both hydrodynamic and thermochemical processes. These models confirm the analyses on the two aspects mentioned above, especially by demonstrating the mutual exclusion between a photoevaporative outflow with appreciable mass-loss rates and a luminous inner-disk [O I] 6300 Å emission consistent with observations.

Some previous works view wind velocities as a criterion for distinguishing different wind launching mecha-

nisms. We nevertheless point out that, due to the analyses about the thermochemical conditions of the coronal gas, both the high-velocity components and the low-velocity components in the TW Hya [O I] emission profiles are *not* the indications of photoevaporative winds. In the case of the low-velocity components observed from transitional disks with lower gas densities ($\lesssim 10^{-3} \times$ full PPDs) and dust abundances, the overall dilemma of photoevaporative mass-loss versus [O I] 6300 Å luminosity (see 2, §4.3) still exists.

In conclusion, consistent co-evolution of non-equilibrium thermochemistry and dynamics (hydrodynamics and MHD) is necessary for physically modeling the outflows of PPDs and plausibly explaining the observed features of disk wind indicators.

Y. Lin and L. Wang acknowledge the computing resources provided by the Kavli Institute for Astronomy and Astrophysics in Peking University. We thank our colleagues for helpful discussions: Gregory Herczeg, Xiao Hu, Haifeng Yang, Xinyu Zheng.

REFERENCES

- Alexander, R. D. 2008, MNRAS, 391, L64
- Alexander, R. D., Clarke, C. J., & Pringle, J. E. 2006a, MNRAS, 369, 216
- . 2006b, MNRAS, 369, 229
- Bai, X.-N. 2017, ApJ, 845, 75
- Bai, X.-N., & Goodman, J. 2009, ApJ, 701, 737
- Bai, X.-N., Ye, J., Goodman, J., & Yuan, F. 2016, ApJ, 818, 152
- Banzatti, A., Pascucci, I., Edwards, S., et al. 2019, ApJ, 870, 76
- Bell, K. L., Gilbody, H. B., Hughes, J. G., Kingston, A. E., & Smith, F. J. 1983, Journal of Physical and Chemical Reference Data, 12, 891
- Black, J. H. 1981, MNRAS, 197, 553
- Chiang, E. I., & Goldreich, P. 1997, ApJ, 490, 368
- Del Zanna, G., Dere, K. P., Young, P. R., & Landi, E. 2021, ApJ, 909, 38
- Dere, K. P., Landi, E., Mason, H. E., Monsignori Fossi, B. C., & Young, P. R. 1997, A&AS, 125, 149
- Draine, B. T. 2011, Physics of the Interstellar and Intergalactic Medium (Princeton University Press)
- Ercolano, B., Clarke, C. J., & Drake, J. J. 2009, ApJ, 699, 1639
- Ercolano, B., & Owen, J. E. 2016, MNRAS, 460, 3472
- Fang, M., Pascucci, I., Edwards, S., et al. 2023a, ApJ, 945, 112
- . 2018, ApJ, 868, 28
- Fang, M., Wang, L., Herczeg, G. J., et al. 2023b, Nature Astronomy, 7, 905
- Font, A. S., McCarthy, I. G., Johnstone, D., & Ballantyne, D. R. 2004, ApJ, 607, 890
- Ge, Q., & Wise, J. H. 2017, MNRAS, 472, 2773
- Gnedin, N. Y., & Hollon, N. 2012, ApJS, 202, 13
- Goldsmith, P. F. 2001, ApJ, 557, 736
- Gorti, U., & Hollenbach, D. 2009, ApJ, 690, 1539
- Gressel, O., Turner, N. J., Nelson, R. P., & McNally, C. P. 2015, ApJ, 801, 84
- Heays, A. N., Bosman, A. D., & van Dishoeck, E. F. 2017, A&A, 602, A105
- Jenkins, E. B., & Tripp, T. M. 2011, ApJ, 734, 65
- Kramida, A., Yu. Ralchenko, Reader, J., & and NIST ASD Team. 2022, National Institute of Standards and Technology, Gaithersburg, MD. <https://physics.nist.gov/asd>
- Meyer-Vernet, N. 2007, Basics of the Solar Wind (Cambridge University Press, Cambridge)
- Mitnik, D. M., & Badnell, N. R. 2004, A&A, 425, 1153
- Murray-Clay, R. A., Chiang, E. I., & Murray, N. 2009, ApJ, 693, 23
- Nemer, A., Goodman, J., & Wang, L. 2020, ApJ, 904, L27
- Omukai, K., Hosokawa, T., & Yoshida, N. 2010, ApJ, 722, 1793
- Owen, J. E., Ercolano, B., Clarke, C. J., & Alexander, R. D. 2010, MNRAS, 401, 1415

- Parker, E. N. 1958, *ApJ*, 128, 664
- Pascucci, I., Cabrit, S., Edwards, S., et al. 2023, in *Astronomical Society of the Pacific Conference Series*, Vol. 534, *Protostars and Planets VII*, ed. S. Inutsuka, Y. Aikawa, T. Muto, K. Tomida, & M. Tamura, 567
- Pequignot, D. 1990, *A&A*, 231, 499
- Picogna, G., Ercolano, B., Owen, J. E., & Weber, M. L. 2019, *MNRAS*, 487, 691
- Rab, C., Weber, M. L., Picogna, G., Ercolano, B., & Owen, J. E. 2023, *ApJ*, 955, L11, (**R23**)
- Riols, A., Lesur, G., & Menard, F. 2020, *A&A*, 639, A95
- Summers, H. P. 2004, *The ADAS User Manual*, version 2.6
- Takeuchi, T., & Lin, D. N. C. 2002, *ApJ*, 581, 1344
- Tielens, A. G. G. M., & Hollenbach, D. 1985, *ApJ*, 291, 722
- Verner, D. A., Ferland, G. J., Korista, K. T., & Yakovlev, D. G. 1996, *ApJ*, 465, 487
- Wang, L., Bai, X.-N., & Goodman, J. 2019, *ApJ*, 874, 90
- Wang, L., & Dai, F. 2018, *ApJ*, 860, 175
- Wang, L., & Goodman, J. 2017, *ApJ*, 847, 11
- Wardle, M., & Königl, A. 1993, *ApJ*, 410, 218
- Xu, R., & Bai, X.-N. 2016, *ApJ*, 819, 68

APPENDIX

A. MEAN FREE PATH OF PARTICLES AND HYDRODYNAMICS

One should prove that the hydrodynamics is applicable to the problem, and the escape of atoms as particles should not be relevant, to justify the arguments based on hydrodynamics. Even if a fraction of gas particles are sufficiently energetic to escape, the mean-free-path of these particles can be estimated (the subscripts “nn”, “nc”, and “cc” indicate neutral-neutral, neutral-charged, and charged-charged collisions, and r_n is the size of the neutral particles; see also [Draine 2011](#)),

$$\begin{aligned}\lambda_{nn} &\simeq 5 \times 10^{-6} \text{ AU} \times \left(\frac{n}{10^7 \text{ cm}^{-3}}\right)^{-1} \left(\frac{r_n}{\text{\AA}}\right)^{-2}, \\ \lambda_{nc} &\lesssim 5 \times 10^{-7} \text{ AU} \times \left(\frac{n}{10^7 \text{ cm}^{-3}}\right)^{-1}, \\ \lambda_{cc} &\simeq 3 \times 10^{-9} \text{ AU} \times \left(\frac{T}{10^4 \text{ K}}\right)^2 \left(\frac{n_e}{10^7 \text{ cm}^{-3}}\right)^{-1}.\end{aligned}\tag{A1}$$

These lengths are tiny compared to the physical scales, which disable the physical picture that the “high-energy tail” of the Maxwell distribution could escape, and assure the applicability of hydrodynamics.

B. THE INEFFICIENCY OF X-RAY HEATING

As one may infer easily by the basic estimations (e.g., §3.1), FUV photons are not sufficiently energetic to launch winds from the inner disk region, and EUV photons cannot penetrate through an [O I] emitting corona to reach the disk surface in the first place. A natural question one may raise is whether X-ray photons are sufficiently energetic to drive photoevaporation from the inner disk. This appendix focuses on the issues regarding the X-ray photons ($h\nu > 0.5 \text{ keV}$), which is also the band elaborated in e.g. [Ercolano & Owen \(2016\)](#) and [R23](#).

B.1. Penetration of the X-ray energy

The penetration of X-ray photons in neutral materials, measured by the column density of neutral hydrogen, is approximately (for $X_O \simeq 3 \times 10^{-4}$),

$$N_H \simeq (\sigma_{O,i} X_O + \sigma_{H,i})^{-1} \simeq 2 \times 10^{22} \text{ cm}^{-2} \times \left(\frac{h\nu}{\text{keV}}\right)^3.\tag{B2}$$

Considering the density profile of a Gaussian disk, $\rho = \rho_0 \exp(-z^2/2h^2)$ (ρ_0 is the mid-plane density), and assume that the materials inside the disk are all neutral.

We have conducted numerical calculations for typical PPD density profile models (in e.g. [Bai 2017](#); [Wang et al. 2019](#)), to find that the following rough estimates yield reasonable approximations of the density at the $\tau = 1$ surface (f is the effective flaring angle of the disk surface),

$$n_{H,\tau=1} \sim \frac{N_H \sin f}{h}.\tag{B3}$$

We find that choosing $\sin f \sim 1/4$ gives no more than $\sim 30 \%$ errors, which is sufficient for the order-of-magnitude calculations in this section.

As the density of neutral hydrogen increases rapidly when approaching the disk mid-plane, the location where the high-energy photons get absorbed roughly satisfies $n_H h \sim N_H$. Given the equilibrium temperature of typical passive PPDs,

$$T_{\text{eq}} \simeq 511 \text{ K} \left(\frac{T_1}{511 \text{ K}}\right) \times \left(\frac{R}{0.3 \text{ AU}}\right)^{-1/2},\tag{B4}$$

and the disk scale height ($\Omega_K = \sqrt{GM_*/R^3}$ is the local Keplerian angular speed; $c_s = \sqrt{k_B T_{\text{eq}}/\mu}$ is the isothermal sound speed; $\mu \simeq 2.35 m_p$ is the average molecular mass, in which we note that the hydrogen atom in molecules can also absorb X-ray via photoionization),

$$\begin{aligned}h &= \frac{c_s}{\Omega_K} \simeq 0.0074 \text{ AU} \times \left(\frac{R}{0.3 \text{ AU}}\right)^{5/4} \\ &\times \left(\frac{T_1}{511 \text{ K}}\right)^{1/2} \left(\frac{\mu}{2.35 m_p}\right)^{-1/2} \left(\frac{M_*}{M_\odot}\right)^{-1/2}.\end{aligned}\tag{B5}$$

The absorption location then roughly has the number density of hydrogen nuclei

$$\begin{aligned}n_{H,\tau=1} &\sim \frac{N_H}{4h} \sim 10^{11} \text{ cm}^{-3} \times \left(\frac{h\nu}{\text{keV}}\right)^3 \left(\frac{M_*}{M_\odot}\right)^{1/2} \\ &\left(\frac{\mu}{2.35 m_p}\right)^{1/2} \left(\frac{R}{0.3 \text{ AU}}\right)^{-5/4} \left(\frac{T_1}{511 \text{ K}}\right)^{-1/2}.\end{aligned}\tag{B6}$$

Such a high density clearly indicates that the absorption location is below the disk surface.

B.2. Equilibrium with cooling

Once the X-ray photons deposit their energy beneath the disk surface, the gas-dust thermal accommodation will play an important role in the thermodynamics. The accommodation rate per gas particle per unit time is approximately (σ_{dust} is the geometric cross section of the

dust grains, and T_{eq} approximates the dust temperature that may be different from the gas temperature T ; see e.g., Goldsmith 2001),

$$\lambda_{\text{dust}} \simeq \left(\frac{8k_{\text{B}}T}{\pi\mu_{\text{H}}} \right)^{1/2} n_{\text{dust}}\sigma_{\text{dust}} \times 2k_{\text{B}}(T - T_{\text{eq}}). \quad (\text{B7})$$

The $n_{\text{dust}}\sigma_{\text{dust}}$ in the equation above can be estimated by $n_{\text{dust}}\sigma_{\text{dust}} \sim (\sigma_{\text{dust}}/\text{H})n_{\text{H},\tau=1}$, where the ‘‘dust cross section per hydrogen nucleus’’ parameter typically takes $(\sigma_{\text{dust}}/\text{H}) \sim 10^{-21} \text{ cm}^2$ (corresponding to a dust-to-gas mass ratio $\sim 10^{-2}$; see e.g., Wang et al. 2019). The mass per particle here is $\mu_{\text{H}} \simeq 0.5 m_p$ as we are estimating the thermal accommodation for the particles right after the ionization.

The cooling by dust grains should be compared to the effects of X-ray photoionization heating. Because the dust temperature T_{dust} is not affected by the irradiation (Appendix B.3), the X-ray heating (γ_{X}) and cooling (λ_{dust}) rates per atom are roughly,

$$\begin{aligned} \gamma_{\text{X}} &\lesssim h\nu(X_{\text{O}}\zeta_{\text{O}} + \zeta_{\text{H}}) \sim 4 \times 10^{-19} \text{ erg s}^{-1} \\ &\times \left(\frac{L_{\text{X}}}{2 \times 10^{30} \text{ erg s}^{-1}} \right) \left(\frac{R}{0.3 \text{ AU}} \right)^{-2} \left(\frac{h\nu}{\text{keV}} \right)^{-3}, \\ \lambda_{\text{dust}} &\sim 4 \times 10^{-19} \text{ erg s}^{-1} \times \left(\frac{T}{T_{\text{eq}}} \right)^{1/2} \left(\frac{T - T_{\text{eq}}}{30 \text{ K}} \right) \\ &\times \left(\frac{R}{0.3 \text{ AU}} \right)^{-3/2} \left(\frac{M_*}{M_{\odot}} \right)^{1/2} \left(\frac{\sigma_{\text{dust}}/\text{H}}{10^{-21} \text{ cm}^2} \right) \left(\frac{h\nu}{\text{keV}} \right)^3. \end{aligned} \quad (\text{B8})$$

In order to stand on the safe side, the expression of γ_{X} overestimates the X-ray heating by assuming that the ‘‘surplus energy’’ ($h\nu - I$) fully goes into the thermal energy of the gas. A more realistic description should include secondary ionization processes due to the collision between energetic electrons and other neutral atoms, which will further reduce γ_{X} drastically.

By equating γ_{X} and λ_{dust} in eqs. (B8), the terminal temperature of the gas at photon energy $h\nu$ can be roughly estimated as,

$$T_{\text{term}} \sim T_{\text{eq}} + 30 \text{ K} \times \left(\frac{R}{0.3 \text{ AU}} \right)^{-1/2} \left(\frac{h\nu}{\text{keV}} \right)^{-6}, \quad (\text{B9})$$

which is approximately valid when the obtained $(T_{\text{term}} - T_{\text{eq}})$ is not greater than T_{eq} . X-ray irradiation with $h\nu = 1 \text{ keV}$, raising the gas temperature only by $T - T_{\text{eq}} \sim 30 \text{ K}$, is far from being sufficient to launch outflows (see the following §3.1). The dust-gas thermal accommodation (appearing to be ‘‘dust cooling’’) will largely offset the maximum possible heating by X-ray. We also note that, if the cooling by atoms and molecules

are included (e.g. Wang & Goodman 2017), the X-ray heating will become even more difficult.

At different photon energy, the physical picture of eqs. (B8), (B9) is clear: the lower the photon energy is, the shallower the radiation can penetrate, the weaker the dust cooling is, and the higher the temperature can reach. This is consistent with existing literature (e.g. Ercolano et al. 2009), that softer ionizing photons are more efficient to produce photoevaporation. These estimations may have caveats for ‘‘soft X-ray’’ photons with $h\nu \lesssim 0.5 \text{ keV}$. For example, solving eq. (B6) for $h\nu = 0.3 \text{ keV}$ gives $n_{\text{H},\tau=1} \sim 3 \times 10^9 \text{ cm}^{-3}$ and $T_{\text{term}} \simeq 10^4 \text{ K}$, which is higher than the sublimation temperature of dust grains. After all dust grains removed, other cooling mechanisms will join the thermal balance at higher temperatures. Considering the $n_{\text{H},\tau=1}$ for these 0.3 keV photons, one can verify that the ionization fraction is low¹, and obtain the cooling rate per hydrogen nucleus $\lambda \gtrsim 10^{-13} \text{ erg s}^{-1}$ at $T \simeq 2 \times 10^4 \text{ K}$ by Lyman- α cooling alone. At lower temperatures such as $T \sim 10^3 \text{ K}$, the energy is removed via the fine structure transitions. For instance, [O I] 63 μm can also overwhelm the heating given $n_{\text{H},\tau=1} > 10^9 \text{ cm}^{-3}$ using the cooling rate coefficient $\Lambda \sim 10^{-26} \text{ erg cm}^3 \text{ s}^{-1}$ at $T \simeq 10^3 \text{ K}$, (Dere et al. 1997; Del Zanna et al. 2021). In fact, the consistent method that was used in e.g. Wang & Goodman (2017) also yields $T \sim 10^3 \text{ K}$ near the $\tau = 1$ surface at $R = 0.3 \text{ AU}$ (not presented in this paper). As we will see in §3.1, this temperature range ($T \sim 10^3 - 10^4 \text{ K}$) is still insufficient to launch winds from the $R \sim 0.3 \text{ AU}$ inner disk regions with considerable efficiency.

B.3. The Impact of X-ray on Dust Temperatures

Is the assumption that ‘‘ T_{dust} is unaffected by the X-ray irradiation’’ reasonable? We note that the dust grains without irradiation are in thermodynamic equilibria with the diffuse infrared radiation (originating from the central star) within the disk (Chiang & Goldreich 1997). For dust grain sizes no smaller than the infrared wavelengths, the Stefan-Boltzmann law constrains the deviation from the equilibrium temperature, leading to the following estimates of the net cooling rates that dust temperature converges to the dust temperature in equilibrium with the diffuse radiation field $T_{\text{dust,eq}} \simeq T_{\text{eq}}$

¹ Assuming a high ionization fraction leads to a $\lambda_{\text{recomb}} \sim 3 \times 10^{-15} \text{ erg s}^{-1}$ recombination cooling rate per hydrogen nucleus at $n_{\text{H}} = 3 \times 10^9 \text{ cm}^{-3}$ and $T = 2 \times 10^4 \text{ K}$, which prevents the runaway heating.

(the subscript “sb” is for the Stefan-Boltzmann law):

$$\begin{aligned} \lambda_{\text{sb}} &\sim 4\pi a_{\text{dust}}^2 \sigma_B (T_{\text{dust}}^4 - T_{\text{dust,eq}}^4) \\ &\sim 0.5 \text{ erg s}^{-1} \times \left(\frac{a_{\text{dust}}}{1 \text{ } \mu\text{m}} \right)^2 \\ &\quad \times \left(\frac{T_{\text{dust,eq}}}{511 \text{ K}} \right)^4 \left[\left(\frac{T_{\text{dust,eq}}}{T_{\text{dust}}} \right)^4 - 1 \right]. \end{aligned} \quad (\text{B10})$$

The maximum amount of heating that this dust grain is “responsible of” can be estimated by,

$$\begin{aligned} \gamma_{\text{dust}} &\sim \left(\frac{\pi a_{\text{dust}}^2}{\sigma_{\text{dust}}/\text{H}} \right) \gamma_X \\ &\sim 3 \times 10^{13} \gamma_X \left(\frac{a_{\text{dust}}}{\mu\text{m}} \right)^2 \left(\frac{\sigma_{\text{dust}}/\text{H}}{10^{-21} \text{ cm}^2} \right)^{-1}. \end{aligned} \quad (\text{B11})$$

The factor 3×10^{13} may seem a tremendous number, but the product with γ_X is still dwarfed by the λ_{sb} , which can eventually cause a temperature raise by $(T_{\text{dust},0} - T_{\text{dust}}) \sim 3 \times 10^{-3} \text{ K}$. If we consider smaller dust grains, the dependence of dust emissivity on temperature will be stiffer (roughly $\propto T^6$). In other words, due to the stiff thermal balance between dusts and diffuse radiation fields in the disks, T_{dust} is not raised by the X-ray irradiation.

C. ISSUES OF DETACHING HYDRODYNAMICS FROM THERMOCHEMISTRY

One may find it curious that, with all the arguments presented in Section §3, why in the first place were the X-ray (and FUV with lower energy photons) driven winds successfully “launched” in some previous works, such as R23 and [Ercolano & Owen \(2016\)](#)? The most prominent issue emerges from the detachment of thermodynamics from hydrodynamics, using a simple mapping of gas temperature T onto the ionization parameter $\xi \equiv F_X/n_{\text{H}}$ ([Owen et al. 2010](#), F_X is the flux of X-ray photons). Recent $\xi - T$ method (e.g. [Picogna et al. 2019](#)) has attempted to break this degeneracy by including the column density as an additional parameter. However, there are still complications unable to be covered by the $\xi - T$ scheme calculated on hydrostatic grids.

Even for the hydrostatic part, the $\xi - T$ scheme could be problematic. Penetration column density of ionizing photons could vary by several orders of magnitude in different energy bands (see also Figure 1), and sometimes there could also be complicated self-shielding and cross-shielding effects inside the PPD corone given the multi-band radiation conditions of the host star (see e.g. [Heays et al. 2017](#) and references therein). The ξ value does not contain the information of photon energy distributions, and the actual ionization rate under the same

ξ could be very different. What is more, the thermodynamics of the gas near disk surfaces can be susceptible to multiple cooling processes. The escape probability of cooling photons, emitted by either molecular coolants (H_2 , OH, H_2O ; see also [Omukai et al. 2010](#)), or atoms and ions (e.g., C II, OI), could vary by several orders of magnitude under the same ξ and lead to very different thermodynamic conditions. Quantifying these processes with a simple ξ could lead to unrealistic outcomes.

Inside the wind, significant heating almost stops due to the lack of neutral materials inside the photoionized wind. Since the photoevaporative winds themselves should always be optically thin to allow high-energy photons to reach disk surfaces, column density corrections do not resolve the problems discussed above either. The adiabatic expansion due to outward motion will cause significant drops in gas temperature. The consideration from the thermodynamic aspect can help us quantify the error that the $\xi - T$ mapping scheme introduces to the system. When converting thermal energy to mechanical energy, the Carnot theorem gives the upper limit of efficiency,

$$\eta < 1 - \frac{T_{\text{low}}}{T_{\text{high}}}, \quad (\text{C12})$$

where T_{low} and T_{high} are the low-end and high-end of the mechanism. To escape from $R = 0.3 \text{ AU}$, we can take $T_{\text{high}} \sim 6 \times 10^4 \text{ K}$. When the gas expands towards the vacuum, as a disk wind eventually does, $T_{\text{low}} \ll T_{\text{high}}$, and thus η is close to unity: the disk wind system converts the thermal energy into mechanical energy with high efficiencies. The $\xi - T$ mapping approach, in contrast, maintains largely invariant gas temperature while increasing the mechanical energy of the system until it’s roughly equivalent to the gas thermal energy. In other words, the total radiation-injected energy could be up to double-counted for adiabatic expansion, one of the fundamental mechanisms that drive the outflow.

Analyses of scalings are helpful in revealing the underlying physics. When a wind fluid element is sufficiently far away from the wind base, its density scales as $n \propto r^{-2}$, where r is its radial location. At that place, the unattenuated radiation flux also scales as $F \propto r^{-2}$. These scalings yield $\xi \equiv F/n \propto r^0$, i.e. the ionization parameter is insensitive to the distance. Insensitive to the distance, the $\xi - T$ mapping technique thus yields largely constant temperature in the winds. According to the Parker wind theory, systems with a polytropic index $\gamma \equiv d \ln P / d \ln \rho < 3/2$ always launch winds, let alone this roughly isothermal condition ([Parker 1958](#); [Meyer-Vernet 2007](#)). Consequently, the $\xi - T$ mapping scheme, by effectively setting $\gamma \simeq 1$, leads to a scenario

in which the winds will *always* be launched no matter what photon energy or luminosity one uses. This is unrealistic, as in reality, there should be no winds when the photon energy is too low or when the luminosity is insufficient. Even when the system manages to achieve constant temperature, the physical parameters required to launch winds with $\sim 10^{-9} M_{\odot} \text{ yr}^{-1}$ mass-loss rates are still mostly unphysical from the $R \lesssim 0.3 \text{ AU}$ part of the disk (see also §3.1, §4). In the most extreme case, the wind base (with high radiation flux and high density) and somewhere in the launched wind (with low flux and low density) might have the same ξ value, but totally different thermochemical conditions such as reaction and cooling rates.